THE ASTROPHYSICAL JOURNAL, 406:306–318, 1993 March 20

THE SOLAR WHITE-LIGHT FLARE OF 1989 MARCH 7: SIMULTANEOUS MULTIWAVELENGTH OBSERVATIONS AT HIGH TIME RESOLUTION

DONALD F. NEIDIG
Geophysics Directorate, Phillips Laboratory (AFSC), National Solar Observatory/Sacramento Peak,[1] Sunspot, NM 88349
ALAN L. KIPLINGER
Astrophysical, Planetary, and Atmospheric Sciences Department, University of Colorado, Boulder, CO 80309; and Space Environment Laboratory, National Oceanic and Atmospheric Administration, Boulder, CO 80303
HOWARD S. COHL[2]
National Solar Observatory/Sacramento Peak, Sunspot, NM 88349
AND
PHILIP H. WIBORG[3]
Received 1992 July 6; accepted 1992 September 24

ABSTRACT

We present observational data for the 1989 March 7 white-light flare (WLF), including *SMM*/HXRBS hard X-ray measurements and CCD optical images in 5000 Å continuum and at 3 Å in the red and blue wings of the Hα line. The optical data were acquired at a 0.5 s rate under good seeing and were further processed to remove image motion and distortion. The flare kernel shows an impulsive rise in both Hα and continuum that is well correlated with impulsive hard X-rays. The Hα emission shows a red asymmetry which we interpret as Doppler redshift associated with explosive heating of the chromosphere. These results are consistent with previous observational descriptions which traditionally have been interpreted in terms of heating and ionization of the flare chromosphere by a nonthermal electron beam. However, new observational results which have not been reported previously include (1) the separation of the flare kernel into a bright inner core and a fainter outer region, where the two components display distinctly different temporal behavior and amount of Hα red asymmetry, and (2) a delay, relative to hard X-rays, of ~1 s in the impulsive rise of the Hα wing emission, followed by an additional 1–2 s delay in the 5000 Å continuum.

It is concluded that the observed fluxes and timing of the hard X-ray and WLF optical emissions are consistent with chromospheric heating by nonthermal electrons, with additional visible light continuum possibly being contributed by a backwarmed photosphere irradiated by intense chromospheric recombination continua (principally Balmer continuum). Power sufficiency of nonthermal electrons in balancing WLF radiative losses is shown to be more easily satisfied when the latter irradiation process applies, than in the case of a purely chromospheric model. The observed delays in impulsive Hα wing emission relative to hard X-rays may be related to the nonthermal ionization time scale of the chromosphere, or may involve the formation of a chromospheric condensation. A satisfactory explanation for the continuum delay is not obtained.

Subject headings: Sun: flares — Sun: X-rays, gamma rays

1. INTRODUCTION

The primary energy release in solar flares in believed to occur in the solar corona. Subsequent transport of energy to the deeper layers of the atmosphere is then required in order to account for the bright chromospheric Hα and other optical flare emission lines. The occasional detection of flare optical continuum, or white-light flare (WLF)—believed to arise in the chromosphere or photosphere, or both—is of particular importance because the radiative losses in optical continuum per unit area and time can be an order of magnitude larger than those in all optical emission lines combined (Neidig 1983, 1989). Therefore the WLF provides a severe test for the mechanisms of flare energy transport that have been proposed thus far (Canfield et al. 1986; Neidig 1989).

Numerous studies of flare Hα emissions have indicated energy transport by nonthermal electrons during the impulsive phase (see review by Canfield et al. 1986). These studies have led to self-consistent models for the highly broadened Stark profiles and redshifts of flare Balmer lines (e.g., Canfield, Gunkler, & Ricchiazzi 1984; Canfield & Galey 1987; Zarro & Canfield 1989). In these models the chromospheric heating and ionization is the direct result of collisional degradation of nonthermal electrons in the dense chromosphere (so-called "thick target" model), producing hard X-rays (by nonthermal bremsstrahlung), and optical emission nearly simultaneously. The simultaneity of these emissions has been tested in several studies using high time resolution (0.3–1.4 s) optical imaging (e.g., Kämpfer & Magun 1983; Kurokawa, Takakura, & Ohki 1988; Wülser & Marti 1989), with the result that the line center Hα impulsive emission rises and peaks virtually simultaneously with impulsive hard X-rays. The latter result is expected on the basis of the very short (<0.1 s) heating time scale in a flare chromosphere bombarded by nonthermal electrons (Canfield & Gayley 1987). Farther in the wings of the Hα line the emission is expected to respond on the somewhat longer (≈1 s)

[1] Operated by the Association of Universities for research in Astronomy, Inc., under cooperative agreement with the National Science Foundation. Partial support for the National Solar Observatory is provided by the USAF under a Memorandum of Understanding with the NSF.
[2] Present address: Department of Physics and Astronomy, Louisiana State University, Baton Rouge, LA 70803-4001.
[3] Same affiliation and postal address as D. F. N.

ionization time scale (Canfield & Gayley 1987). However, previous observations in the line wings have been made either too close to line center or at lower time resolution; consequently the predicted delay in Hα wing emission has not been adequately tested. On the other hand, the co-spatial relationship between Stark-broadened, redshifted Hα emission, and intense hard X-ray emission has been confirmed, at least to the 8″ resolution available with the *SMM* Hard X-ray Imaging Spectrometer (Canfield & Gunkler 1985). Thus some direct observational evidence supports models of chromospheric heating by nonthermal electrons in the flare impulsive phase.

Extending the above model to the production of optical continuum in WLFs, however, is not yet established. Basic questions remain with regard to sufficiency of energetic electron penetration depth in the atmosphere (owing in part to uncertainty in the atmospheric height of the WLF), energy deposition rate, and timing of white-light emission relative to hard X-rays. While it is clear that the WLF is at least roughly associated with the flare impulsive phase and is in all cases accompanied by strong emission in hard X-rays (Canfield et al. 1986; Neidig et al. 1989), the exact timing relationship has been obscured by poor time resolution of the optical measurements (never better than 10 s and often as poor as 30 s) or by large photometric errors suffered by photographic recording. Neidig & Kane (1993) found that in all cases where simultaneous multiwavelength optical photometry and hard X-ray measurements were available, sufficient power was present in nonthermal electrons above ~50 keV to balance the power radiated in optical continuum at the time of WLF maximum. Electrons with energies above 50 keV can penetrate well into the chromosphere, thus making nonthermal electrons a candidate heating mechanism for continuum sources in the chromosphere. Yet the validity of this model depends on more stringent tests of power sufficiency of nonthermal electrons, as well as temporal relationships between impulsive hard X-ray and optical emissions, using precise optical photometric measurements at high time resolution.

The optical data presented herein are unique in several respects. The images were acquired under good (≤1″) seeing with high time resolution (0.5 s) and high photometric accuracy afforded by CCD detectors. The well-defined impulsive phase of the March 7 WLF provided a reliable fiduciary for temporal comparisons; and the flare was observed in spatially unresolved hard X-rays by the *SMM* Hard X-ray Burst Spectrometer (HXRBS). In § 2 we present the data, paying special attention to energetics and relative timing of optical and hard X-ray emissions. We then demonstrate in § 3 that difficulties arise in attempting to interpret the optical continuum as purely chromospheric in origin, within the context of heating by nonthermal electrons, and that these difficulties might be substantially removed if part of the continuum is produced in the photosphere as a result of backwarming by the flare chromospheric continuum.

2. OBSERVATIONS AND DATA ANALYSIS

The 1989 March 7 flare (maximum 1455 UT; Hα/soft X-ray class 2B/X1.8; location N32/E65; heliocentric angular distance $\theta = 76°$) was one of numerous major events, including several other WLFs, that occurred in the highly active region NOAA 5395. The flare was observed at Sacramento Peak in CCD optical images at three wavelengths by the Vacuum Tower telescope, in photographic images at two wavelengths by the Multiband Patrol, and in spatially unresolved hard X-rays by *SMM*/HXRBS. Below we describe the optical and HXRBS data and the general characteristics of the flare, and present a detailed comparison between optical and hard X-ray time profiles and energetics.

2.1. *Optical and Hard X-Ray Data*

Images of the flare were obtained at the Vacuum Tower telescope with a time resolution of 0.5 s in three bands, using beamsplitters, filters, and three thermoelectrically cooled RCA 504 CCD arrays which were exposed simultaneously. We selected one band (5000 Å, bandpass 50 Å) in which the flare emission would be dominated by continuum in a white-light flare, and two 0.25 Å bands in the wings of the Hα line: 3 Å in the blue wing, obtained with the Universal Birefringent Filter (UBF), and 3 Å in the red wing with a Zeiss tunable Hα filter. The contribution by chromospheric or other flare-excited lines within the 50 Å bandpass of the 5000 Å filter is expected to be relatively small in comparison to the WLF continuum[4]; therefore, we refer to the flare emission in the 5000 Å filter as "continuum," although the measurements of the flare continuum intensity enhancement in this band should rightly be treated as overestimates. The images in each wavelength were digitally recorded on high-speed tape drives along with the Universal Time when each image was acquired. A time standard (accurate to better than 1 ms as received at Sacramento Peak) was obtained from nearby White Sands Missile Range. A delay of 35 ms in the hardware overhead and electronic shutter has been corrected in the displays. The final focal plane image scale was 1″ pixel^{-1} in both dimensions, with 120 × 72 pixels being read out as a subarray.

The data reduction included corrections for CCD gain and dark current, and flat field (CCD fringe removal). Flare intensities were obtained by calibrating the images against the quiet sun background, for which the intensity in each of the filter bandpasses is known from absolute irradiance measurements (e.g, Allen 1973) and published atlases (e.g., Beckers, Bridges, & Gilliam 1976). We applied a correlation tracking routine in order to remove atmospheric seeing motion and to coregister each image relative to an arbitrarily chosen reference image in the time series. This technique divides each image into a number of disjoint, small subarrays, each of which is individually cross-correlated and coregistered with its associated subarray in the reference image. The x-y offsets for each of the subarrays are then used to fit a two-dimensional polynomial over the entire image. This gives a mapping by which each pixel on a regular grid in the output (corrected) image may be interpolated from typically 4 pixels in the input (distorted) image (Niblack 1986). We derived the mapping from the continuum image only, then applied it to all three images of each set. Although this correlation tracking technique has the effect of slightly smoothing some of the intensity peaks in the image, a significant advantage is gained in the comparative photometry of small features by reducing noise that otherwise would have resulted from geometric distortion and low-frequency image motion.

[4] The spectrum of a WLF of comparable brightness—1981 April 24 (Neidig 1983)—revealed six metallic absorption lines between 4950 and 5050 Å that reverted to emission or showed central reversal in their cores during the flare. The total emission from five of these lines was negligible relative to the WLF continuum in this band. The sixth line (Fe II 5018 Å), however, was approximately as bright as the He 5016 Å line which ordinarily appears in emission in highly energetic flares. Together, the latter two lines contributed 1.3 × 10^6 ergs s^{-1} cm^{-2} sr^{-1}, or ~7% of the total observed flare intensity in a 50 Å band at 5000 Å.

In addition to the CCD data, photographic images were acquired with the Sacramento Peak Multiband Patrol (MBP) telescope (Neidig & Beckers 1983) in wavelengths/bandpasses of 3610/22 and 4275/40 Å at a time resolution of 15 s. Although the seeing was generally good, chromatic aberration in the MBP produces a soft focus in the 3610 Å image. Photometric reduction of the MBP images was accomplished with a Joyce-Loebl microdensitometer, using a series of linear scans aross the flare image, and converting photographic density to intensity to obtain the spatial distribution of flare intensity relative to background.

The full Sun X-ray measurements were acquired with the HXRBS scintillation counter (Orwig, Frost, & Dennis 1980) at 0.128 s time resolution in 15 energy channels covering 52–856 keV; the drift of these channels toward higher energy, through detector aging, was taken into account. Here, the HXRBS data have been averaged to produce 0.512 s sample intervals that are comparable to the time resolution of the optical data. The observed counting rates are reproduced by folding through the detector sensitivity (e.g., Schwartz et al. 1991) a best-fit power-law photon spectrum $J = A(h\nu)^{-\gamma}$ photons s^{-1} cm^{-2} keV^{-1} at 1 AU, where $h\nu$ is the photon energy (keV).

Short duration fluctuations seen in time profiles of the photometric data generally consist of only one or two individual data points, and there is no significant correlation between fluctuations in hard X-rays and optical emissions on time scales ≤ 1 s, even when time delays are introduced in the X-ray data (see § 2.3 below). Coincident fluctuations are observed in the time profiles of the three optical wavelengths, but these are most likely due to correlated seeing disturbances. Concluding, therefore, that the short duration fluctuations can be treated as noise, we removed frequencies above 0.2 Hz in the Fourier filtered renditions of the data. Prior to filtering, we interpolated across gaps (6 data points per gap) in the optical data that occur every 60 s between data files. No gaps occurred during the flare impulsive rise.

2.2. *Description of the Flare*

The March 7 flare was complex, displaying a number of kernels which varied rapidly with time. The vast majority of flares are not visible at 3 Å from Hα line center, and even in the brightest flares the emission in the far wings appears only in the most intense kernels. Thus the March 7 event, which showed numerous kernels as well as a substantial portion of its two-ribbon Hα structure at 3 Å from the line center, was somewhat exceptional. Figure 1 shows CCD images in Hα +3 Å

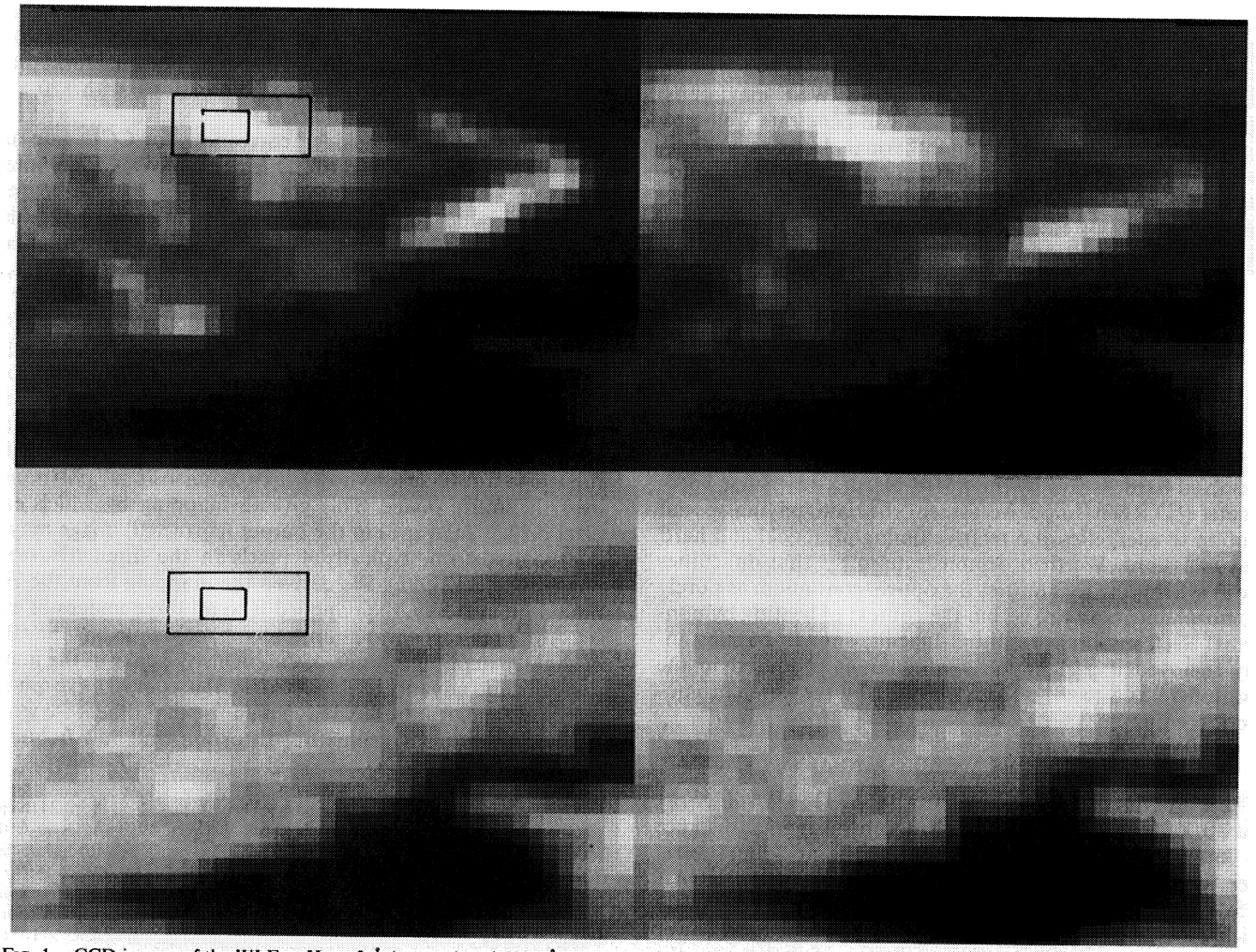

FIG. 1.—CCD images of the WLF at Hα +3 Å (*top row*) and 5000 Å continuum (*bottom row*) at 14:55:14.5 UT (*left column*) and 14:55:31.0 UT (*right column*), covering a field of view 41″ × 31″. Subarrays selected for photometry (inner core and outer region) are shown by rectangles. The direction to the solar limb is toward the top.

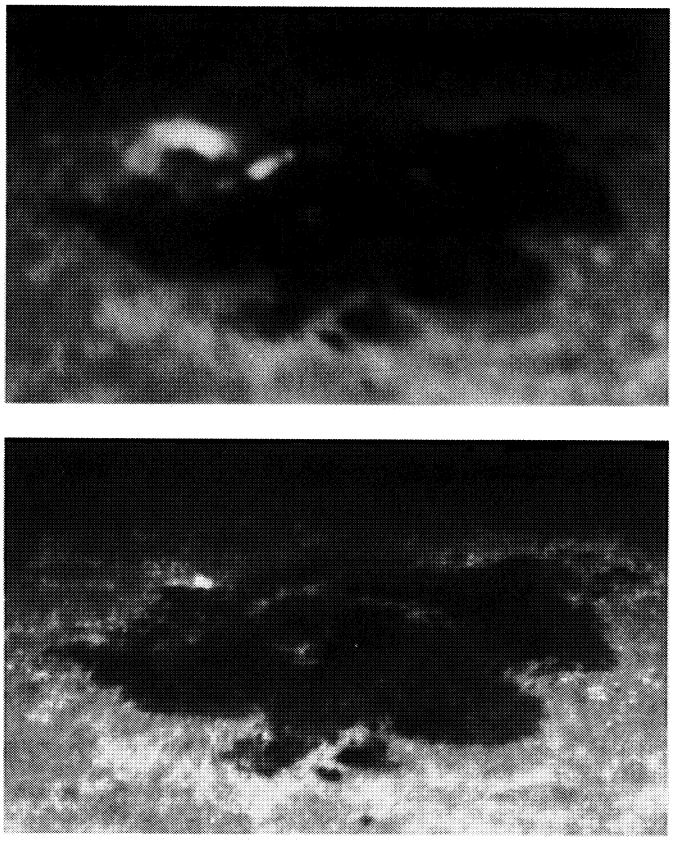

FIG. 2.—Multiband patrol images of the WLF; the field of view is 178″ × 106″ and the solar limb is at the top. *Top:* 3610 Å (14:55:30 UT; *bottom:* 4275 Å (14:55:15 UT). The soft focus in the 3610 Å image is due to chromatic aberration.

and 5000 Å continuum near the time of WLF peak intensity. The photographically recorded 3610 Å continuum emission (Fig. 2) is brightest and most extensive just outside the sunspot penumbra, and coincides with the location of the kernel visible at 5000 Å. It is presumed that this principal WLF emission source lies in a region of weaker magnetic field than the smaller, less bright patches that are visible only at 3610 Å and which are situated close to the umbra.[5] The occurrence of the more intense optical emission in the flare ribbon or footpoint located in the weaker field is relatively common, and supports a flare model with enhanced precipitation of high-energy particles (via larger loss cone) from a bipolar magnetic loop at the footpoint of weaker field (Neidig 1981; Nitta, Kiplinger, & Kai 1989).

The photometry of the CCD digital images was restricted to the main flare kernel visible in 5000 Å continuum, where in Figure 1 we define a bright *inner core*, 2″ × 3″ in extent, surrounded by a less bright *outer region* with dimension 4″ × 9″. The corresponding areas on the Sun, corrected for foreshortening, are 1.3×10^{17} and 6.5×10^{17} cm^2 (the latter with the inner core subtracted off); these are adopted as the respective areas of the WLF emission for the two components of the kernel and are further assumed to be identical to the respective

[5] It is believed that the large emission patch lies in photospheric field of polarity opposite to the two small patches near the umbra; however, this is difficult to confirm from magnetograms, due to projection effects on the magnetic field near the solar limb.

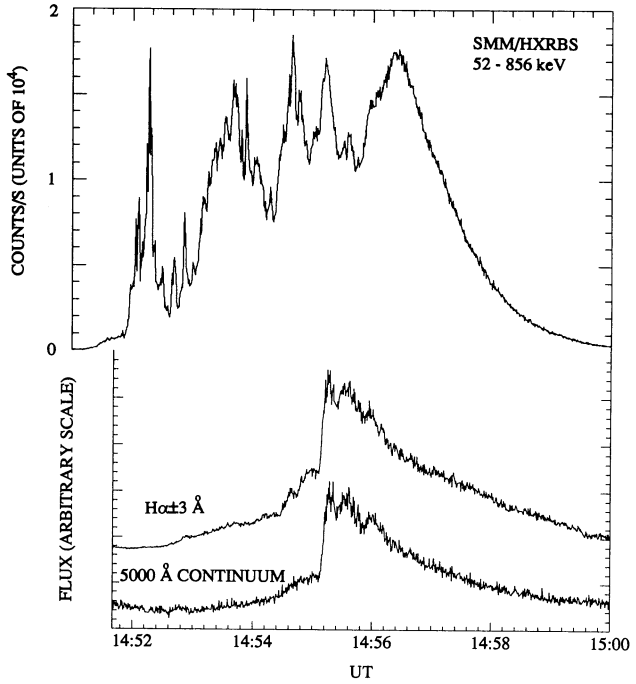

FIG. 3.—Time profiles in hard X-rays, Hα ±3 Å intenisty in the inner core, and 5000 Å continuum intensity in the inner core.

electron beam cross sections, in subsequent discussions of chromospheric heating via nonthermal electrons. The Hα photometry was performed on identical areas in the corresponding coregistered Hα images. Below, we show that the temporal and spectral behavior of these inner and outer components are distinct from one another, and discussions of their characteristics will occupy a considerable part of the interpretation in § 3.

Reflecting the optical intensity and complexity of the March 7 flare, the hard X-ray profile (Fig. 3) reveals large, multiple, impulsive features, most of which were temporally associated with one or more Hα kernels. The hard X-ray photon spectral index γ varied over the range 3.6–7 during the flare, reaching its minimum (hardest spectrum) at 14:54:30 UT (the spectral parameters γ and A are defined in § 2.1). At the time of peak intensity in the WLF (14:55:15 UT), $\gamma = 5.2$, and the X-ray spectral parameter $A = 6.8 \times 10^9$. It is interesting that, of the numerous hard X-ray features in the March 7 event, the one associated with the WLF had neither the largest flux nor the hardest spectrum.

2.3. *Optical and Hard X-Ray Time Profiles*

Figure 4 shows the time profiles at Hα ±3 Å (red and blue wing intensity average) and 5000 Å continuum, where in each of these wavelengths we see a different temporal evolution between the inner core and outer region of the flare kernel. The fast rise, or "impulsive," component is more pronounced in the inner core, while in the outer region a gradual component peaking 15–20 s after the impulsive phase dominates the emission. Also, a preimpulsive gradual rise is evident in both inner core and outer region.

A difference is also apparent in the asymmetry of the Hα wing emission (Fig. 5), with the outer region gradual peak showing blue excess and the inner core showing red excess during the impulse peaks (14:55:15, 14:55:30, and 14:55:36

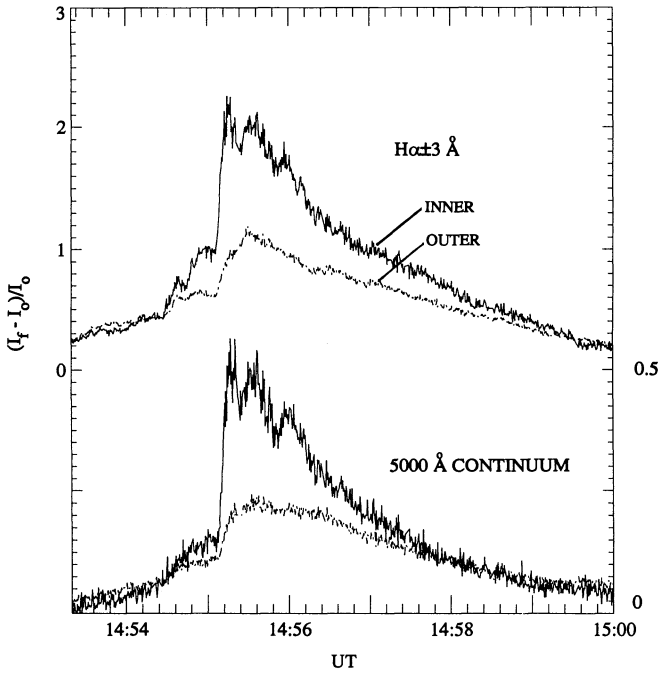

FIG. 4.—Time profiles for the inner core and outer region, in Hα ±3 Å (*top, read left scale*) and 5000 Å continuum (*bottom, read right scale*).

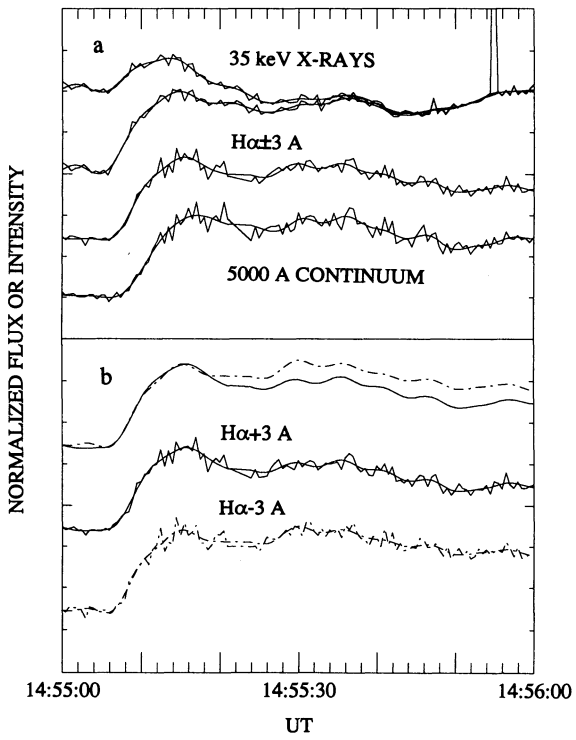

FIG. 6.—Comparison of Fourier-filtered and unfiltered time profiles during the impulsive phase. (*a*) 35 keV X-rays (top curve without, and second curve with, the subtraction of an assumed exponential decay of the previous X-ray burst structure), Hα +3 Å averaged with Hα −3 Å (third curve), and 5000 Å continuum (fourth curve). (*b*) Individual time profiles in Hα +3 Å (*solid curve*) and Hα −3 Å (*dash-dotted curve*); the top two curves show the Fourier-filtered profiles superposed. All curves in this figure are shown on arbitrary scales of intensity, and all (except the topmost X-ray profile) have been normalized between their respective preimpulsive minima and impulsive phase maxima.

UT) as well as during the preimpulsive rise. The red asymmetry is discussed below in connection with its well-known interpretation (e.g., Canfield & Gayley 1987) as a Doppler-shifted line profile resulting from downward motion of a chromospheric condensation in response to explosive flare heating above the Hα source. On the other hand, the blue asymmetry observed in the outer region appears to have been caused, in part, by a

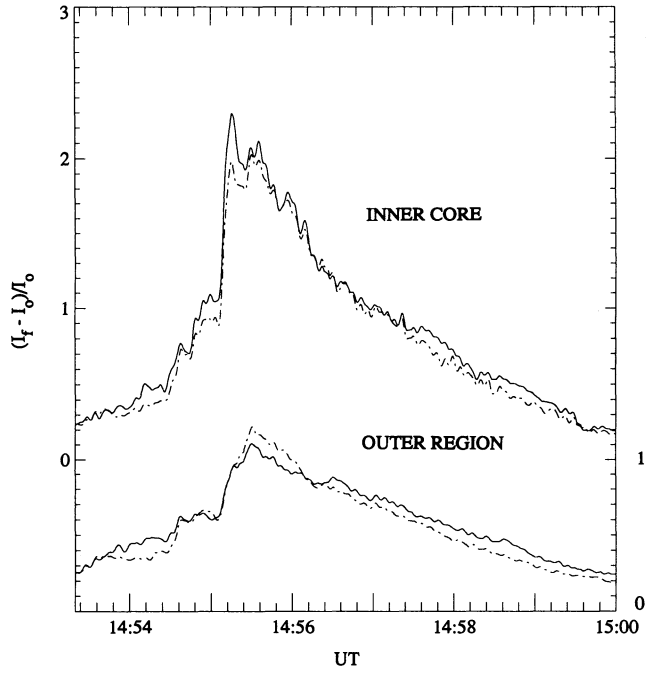

FIG. 5.—Fourier-filtered time profiles in Hα +3 (*solid curves*) and Hα −3 Å (*dash-dotted curves*) in the inner core (*top, read left scale*) and outer region (*bottom, read right scale*).

tuning error in the UBF 0.5 Å element which produced a spurious sideband in the transmission profile at Hα −2.5 Å when the central transmission was tuned to Hα −3 Å.[6] In the case of a nonredshifted or weakly redshifted Hα flare emission line, this sideband would have resulted in a brighter flare image through the UBF (blue wing image) simply as a consequence of the strong spectral intensity gradient in the flare line profile. Despite this blue bias, the fact that a red asymmetry was observed in the inner core, leads us to conclude that the inner core line profile was quite strongly redshifted. In view of our lack of information on the detailed shape of the flare Hα line profile we are unable to correct the blue bias or to infer velocities from the observed asymmetries.

The 35 keV photon flux near the time of peak white-light emission is shown on an expanded time scale in Figure 6*a*. The X-ray data are presented in two ways: the topmost curve shows the 35 keV photon flux directly while the second shows the effect of subtracting an assumed exponential decay of the burst structure previous to the WLF (see Fig. 3). Beginning at time t_0 = 14:55:05.7 UT we subtract from the observed X-ray flux (or electron power, in subsequent discussions) an amount $X(t_0)e^{-\Delta t/9.73}$, where $X(t_0)$ is the observed flux or electron

[6] A possible additional contributor to the observed asymmetry is the effect of the different orientations of the entrance polarizers of the two filters on Hα flare emission which might have been partially polarized by particle beam impact (see Henoux 1991). The experiment described here was not set up to account for polarized light variations in the incoming beam.

power at time t_0 and Δt is the time in seconds after t_0. The rationale for choosing this particular decay function is that it produces the best fit between the optical and X-ray profiles. Even so, this fit becomes poorer at higher photon energies, due to the more rapid decay generally observed at higher X-ray energies during the decay phase of impulsive X-ray features. In addition to reducing the X-ray photon flux and nonthermal electron power by ~25% at the peak of the WLF impulsive phase, the subtraction of the exponential decay produces small effects on the timing of X-ray features (compare first two curves in Fig. 6*a*). In particular, the impulsive rise, in the mean, occurs 0.5 s *later* than the rise in the unmodified X-ray profile. Later X-ray peaks show negligible shifts because the effect of the exponential substraction becomes unimportant. In the absence of spatially resolved hard X-ray emission it is impossible to know which of the two X-ray profiles should be used for temporal comparison with optical light curves. We must concede, therefore, that the true times of onset and peak of the WLF-associated X-rays cannot be known to any better precision, and that, in general, there exists an inherent uncertainty in the timing of fluxes from multiple sources that are spatially unresolved.

The time profiles of the impulsive inner core Hα ±3 Å (red and blue wing average) emission and 5000 Å continuum are shown in the third and fourth curves of Figure 6*a*. It is important to note, in the interpretations below, that there is no measurable difference between the time profiles in the red and blue Hα wings when the intensities are normalized between their respective preimpulsive minima and first impulsive maxima (Fig. 6*b*).

Generally, the optical profiles of Figure 6 bear considerable similarity to the 35 keV X-ray profile with the subtracted exponential decay. There is, however, a small delay in the Hα ±3 Å profile, and a larger delay in the 5000 Å continuum profile, relative to the hard X-ray profile. These delays are better shown in Figure 7, where the normalized filtered profiles of all three impulsive phase emissions are superposed. In the inner core the mean lag in the Hα ±3 Å profile is 0.8 s, which exceeds the time resolution of the observations; and although the amount of the delay can be made to vary slightly, depending on the choice of filtering parameters, it cannot be made to vanish (note that the lag is even greater—approximately 1.3 s—if we used the unmodified X-ray profile). The mean lag in the continuum is quite obvious and amounts to ~2.5 s. Later peaks in the flare show little or no measurable lag in Hα ±3 Å or continuum relative to hard X-rays. In the outer region of the flare kernel the order of the delays during the impulsive rise is the same as in the inner core, although the mean lags are longer: 1.8 and 3.1 s, respectively. After the impulsive rise the outer region optical emissions continue to increase, while the hard X-rays do not. Unlike the optical fluxes from the inner core, the correlation between the Hα wing and continuum emissions during the postimpulsive phase is relatively poor. Any hard X-ray component correlated with the gradual optical emissions, if it exists, is masked by the presence of the impulsive components.

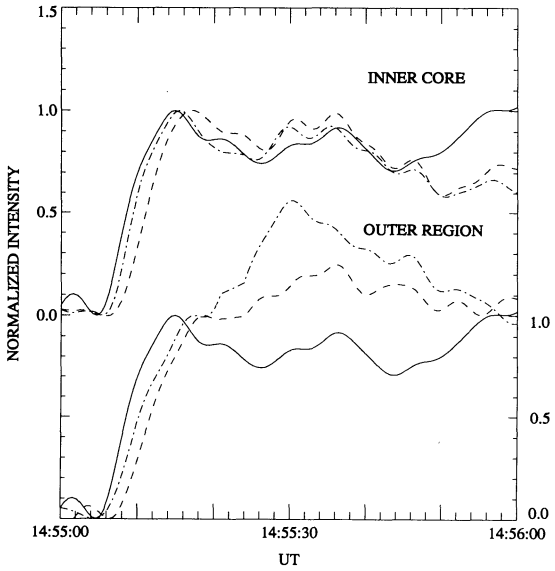

FIG. 7.—Detailed comparison of the normalized, Fourier-filtered time profiles in 35 keV X-rays (*solid curve*), Hα ±3 Å (*dash-dotted curve*), and 5000 Å continuum (*dashed curve*), for both inner core (*top, read left scale*) and outer region (*bottom, read right scale*).

2.4. *WLF Spectrum and Energetics*

Typical of most WLFs, the March 7 event was much brighter in Balmer continuum than in visible wavelengths. Although some of the emission in the 3610 Å MBP image is attributed to numerous weak lines (see spectra, for example, in Neidig 1983), the relatively large Balmer contribution can hardly be doubted in this WLF. In view of the effect of chromatic aberration (§ 2.1) on peak intensity, the relative flare brightnesses at 3610 and 4275 Å are best compared by means of spatially integrated intensities, or flux enhancements per unit wavelength interval ($F_{\text{flare}} - F_{\text{background}}$). Thus we find an enhancement ~8 times larger at 3610 Å in the main kernel (inner core and outer region combined), subject to an uncertainty of perhaps several tens of percent.

The total WLF power in near-ultraviolet, visible, and near-infrared continua at flare maximum is obtained by integrating the intensity over wavelength and one hemisphere of solid angle. This requires a model for the optical emission. In the discussions below we favor an irradiation model consisting of both chromospheric and photospheric components (§ 3.2 and Appendix). The spectrum and variation of flare intensity with viewing angle, computed from this model, then leads to an estimate for the total power (see Appendix) consistent with the observed intensity at 5000 Å (we refer to the CCD measurements as being more reliable in scaling the wavelength-integrated flare emission from the model). For the fainter kernels, which are not visible at 5000 Å, the outputs relative to the main kernel are estimated by comparing the ratios of their spatially averaged 3610 Å intensities with that of the main kernel, using the MBP 3610 Å images which reveal the fainter kernels. The results are summarized in Table 1.

The thick target nonthermal electron power at the Sun above electron cutoff energy E_0 (keV) is (Brown 1971; Lin & Hudson 1976):

$$P_e(E \geq E_0) = 9.44 \times 10^{24} b(\gamma) A(\delta - 2)^{-1} E_0^{2-\delta} \text{ ergs s}^{-1}, \quad (1)$$

where A and γ are the observed X-ray spectral parameters (defined in § 2.1), δ ($=\gamma + 1$) is the electron spectral index, and $b(\gamma)$ is a function plotted in Lin & Hudson (1976). [The function $b(\gamma)$, which involves γ as well as a β-function in γ, arises from the inversion of the equation for nonthermal bremsstrahlung in deriving the electron spectrum.] Because the radiative losses in the WLF optical continuum are generally known to

exceed losses in Balmer and other chromospheric lines by a large factor (Neidig 1989), we proceed on the assumption that all the power in thick target nonthermal electrons is being deposited within the WLF. After subtracting the assumed contribution to the X-ray flux by the previous burst structure (§ 2.3) the resulting power in nonthermal electrons at the 14:55:15 UT impulsive peak, above cutoff energies 48 and 60 keV, is 38.1×10^{27} and 14.9×10^{27} ergs s^{-1}, respectively (the choice of these particular cutoff energies is made according to the atmospheric heights characteristic of the chromospheric optical continuum sources, as derived in § 3.3). We apportion 0.72 of this electron power to the main kernel, according to the same ratio as derived from the observed optical outputs and similarly divide the resultant electron power between the inner core and outer region (Table 1). It is worth noting that the corresponding fluxes in nonthermal electrons above 20 keV, assuming electron beam cross sections equal to the WLF areas (§ 2.2), are $F_{20} = 2.8 \times 10^{12}$ and 1.1×10^{12} ergs s^{-1} cm^{-2}, respectively, in the inner core and outer region. These are an order of magnitude larger than input fluxes assumed in electron heated flare atmospheric models published to date.

3. INTERPRETATION OF OBSERVATIONAL DATA

In this section we attempt to determine the consistency of models of chromospheric heating by nonthermal electrons with the salient features of the observational data. As a result of several aspects of WLF observations which traditionally have proven troublesome to understand—in particular, questions of the WLF atmospheric regime and the heating mechanism(s)—it is necessary to engage in several preliminary discussions.

3.1. Hα *Redshifts*

Figures 5, 6, and 7 together demonstrate the classic signatures of nonthermal electron heating of the flare chromosphere: close association between impulsive phase hard X-rays and Hα emissions, and impulsive phase redshifted Hα profiles[7]. These signatures are most pronounced in the inner core. (Anticipating that the observed short delays in the optical emissions relative to hard X-rays during the impulsive rise might be expected as a result of heating and ionization processes, we ignore these timing differences for the moment.) In the outer region the impulsive phase signatures are less distinct; in particular, the measured intensities in Hα blue and red wings are virtually identical at the impulsive peak (14:55:15 UT). Recalling, however, the blue bias in the measurements (§ 2.3) it is concluded that the Hα profile at this time and location must actually be redshifted, although to a lesser degree than in the inner core. At the Hα gradual peak (14:55:30 UT), however, the outer region shows a marked blue asymmetry, and in view of the unknown bias we are able to conclude only that the redshift, if present at all, is even smaller than in the outer region impulsive phase.

[7] Curiously, episodes of Hα red asymmetry are also observed at times and places other than the principal impulsive phase structures. Some, but perhaps not all, of these may be associated with hard X-ray features. Compare, for example (Figs. 3 and 5), the X-ray structures associated with the redshift episodes in the outer region at 14:53:40–14:54:40 UT and at 14:56:30 UT, and in the core at 14:54:12, 14:55:00, and 14:57:30 UT. Note that the onset of the latter episode does not correspond with any X-ray feature. Also, the long duration redshift appearing in the decay phases of both the core and the outer region may be associated only with the large, thermal-like X-ray feature (Fig. 3) that dominates the X-ray emission at low photon energies after 14:56 UT.

TABLE 1

SUMMARY OF ENERGETICS[a]

Flare Kernel Location	Peak WLF Power[b]	Electron Power[c]	
		≥48 keV	≥60 keV
All WLF kernels	15.5	38.1	14.9
Main WLF kernel	11.2	27.4	10.7
Inner core	3.7	...	3.6
Outer region	7.5	18.2	...

[a] In units of 10^{27} ergs s^{-1}.

[b] Peak power radiated in near UV, visible, and near-IR continua at the impulsive phase peak (14:55:15 UT), assuming the emergent intensity is distributed over wavelength and viewing angle according to the irradiation model (see § 3.2 and Appendix); these outputs are slightly larger if a purely chromospheric model is assumed.

[c] Power is given above cutoff energies required for electrons to reach chromospheric levels characteristic of the irradiation model (§§ 3.2 and 3.3) for both inner core and outer region.

In the inner core the red asymmetry is present prior to the onset of the main impulsive phase (Fig. 5), and although the difference between the red and blue wing intensities increases during the impulsive rise and first impulsive peak, this difference remains approximately proportional to the intensity. This is further demonstrated in Figure 6, where we see that the individual Hα +3 and Hα −3 Å emissions, when normalized between their respective preimpulsive minima and first impulsive peaks, are virtually indistinguishable from one another throughout their onset and rise to maximum intensity. This remarkable similarity is not evident in wing intensities derived from hydrodynamic models (see Fig. 2 of Canfield & Gayley 1987), where the development of a redshifted chromospheric condensation introduces different time behaviors in the red and blue wings during the first few seconds of the impulsive rise. (Failure to observe these differences here may be related, in part, to noise in the unfiltered data, insufficient time resolution in the filtered data, and ramped increase in the heating function, which differs from the truly impulsive heating function assumed in the Canfield & Gayley computations.) Instead, the observations here are consistent with a *constant* redshift (present even in the intensity plateau prior to the main impulsive rise), combined with increasing line width and/or intensity during the impulsive rise.

The observed temporally symmetric increase in impulsive phase red asymmetry at ±3 Å in the Hα wing indicates that the full width of the Doppler-shifted portion of the inner core line profile must exceed 6 Å. This is substantially wider than the shifted profiles computed by Canfield & Gayley (1987) and suggests that the density in the moving condensation is initially quite large, implying an origin of the condensation at relatively great depth in the chromosphere. This further implies explosive heating at an atmospheric depth greater than heretofore considered in flare models. Considering the very large electron flux that applies in the March 7 flare (nearly two orders of magnitude larger than assumed by Canfield & Gayley), this might not be surprising. Finally, as chromospheric condensations are characterized primarily by the density enhancements they produce (Fisher, Canfield, & McClymont 1985b), the existence here of a highly broadened redshifted profile may be significant in relation to estimates of flare densities derived below.

3.2. *Models for Optical Flare Emission*

Two simple models for optical flare emission are presented here. Although these do not incorporate all of the physics that

has been included previously in detailed flare models, we refer to them for benchmark comparisons in the discussions below, particularly in demonstrating how various aspects of the observations here might be consistent with chromospheric heating by nonthermal electrons.

Flare emission in the Hα line is accepted as originating in a relatively thin chromospheric slab, typically 100 km in thickness, with temperature nominally 10^4 K (e.g., Svestka 1965). A thin layer (approximately one density scale height) for the Hα source happens also to be a feature of chromospheric heating by an electron beam (e.g., Gayley & Canfield 1991). At 10^4 K the chromosphere is substantially ionized, and the resulting ion electric fields produce strong Stark broadening of the Balmer emission lines. Thus the opacity in the far wing of Hα can be expressed in terms of the local electron density. Electron densities $n_e > 10^{13}$ cm^{-3} are required in order to produce the observed Balmer line spectra in large flares. In the case of WLFs, any optical continuum produced in the chromosphere at temperatures near 10^4 K must be due primarily to hydrogen recombination (H_{fb}) and, to a lesser extent, thermal bremsstrahlung (H_{ff})[8]. Like the Hα wing emission, these continua are strongly dependent on the electron density and are therefore highly sensitive to ionization in the chromosphere. The objective of the models here is to estimate the electron density in the optical source, given observations of the Hα wing and 5000 Å continuum intensities.

We approximate the chromospheric component of the flare by a homogeneous slab of uniform density and temperature, with vertical extent equal to the quiet chromosphere density scale height (130 km). Two chromospheric flare temperatures, T_c, of 10,000 or 15,000 K, are assumed in the computations. Radiative source functions and slab optical thicknesses in Hα line and H_{fb} continua are calculated with the aid of density-dependent second- and third-level hydrogen departure coefficients interpolated from tables published by De Feiter (1966), which include a grid of conditions relating to the internal radiation field. Hydrogen levels ≥ 4 are taken to be in LTE, which is a good approximation at the electron densities encountered here. For the optical thickness in the Hα wing we use equation (67) of Svestka (1965), which includes the effects of Stark broadening. The H_{ff} continuum is taken to be in LTE. Under these conditions and assumptions the electron density n_e remains as the only free parameter required in calculating the chromospheric contribution to the flare intensity for the wavelengths of interest. In calculating the emergent flare intensity we enter incident photospheric intensity on the slab from below, and use the radiative transfer equation for a homogeneous medium (see eq. [A8] in the Appendix). The H_{fb} and H_{ff} spectrum for the 10^4 K case is shown in Figure 8 in the Appendix. This adopted model is static and cannot account for the impulsive phase flare dynamics that are included in hydrodynamic flare models. Our purpose here, however, is limited primarily to obtaining estimates for the required chromospheric density in the WLF and the resulting emergent flare spectrum.

[8] The presence of the H_{fb} component in WLFs has been confirmed by the existence of Balmer or Paschen continuum edges in a number of WLFs. In other cases the continuum edges—the Balmer jump, in particular—are below a detectable level (Boyer et al. 1984; Machado et al. 1986; Mauas 1990). The nonexistence of Balmer continuum is incompatible with the models described here. A novel explanation, however, for the absence of *observable* Balmer continuum, owing to a chromospheric condensation having a radiative source function approximately equal to the background photospheric intensity, is presented by Gan et al. (1992).

The above model, which is purely chromospheric, ignores the effect of the flare radiation on the underlying atmosphere. Irradiation of the photosphere, however, is inevitable and non-negligible in any case where an intense optical source exists in the chromosphere. The concept has been discussed in connection with WLFs by Machado, Emslie, & Avrett (1989) and Hawley & Fisher (1992). In these models the chromospheric continua are absorbed in the photosphere where they produce a small temperature rise (of order 10^2 K). Photospheric energy balance is then restored by enhanced radiation by the H^- ion. The latter radiation will be roughly Planckian in form with characteristic temperature near 6000 K. A key feature of this irradiation mechanism is that the Balmer continuum, which carries $\sim\frac{2}{3}$ of the chromospheric flux (when the chromospheric temperature is 10^4 K; see Fig. 8) is effectively converted into visible light continuum. The relative contributions to the flare intensity by the chromospheric and photospheric components are strongly dependent on viewing angle θ (see Fig. 9); at 5000 Å amd $\theta = 76°$, each contributes approximately equally to the total flare intensity when the chromospheric temperature is 10^4 K.

The two models above—which we refer to as the purely chromospheric model and the irradiation model—make different predictions for the ratio of flare Hα ± 3 Å line to 5000 Å continuum emissions which can be compared with observation (below we express the flare emissions in terms of the intensity enhancement, $I_f - I_o$, per unit wavelength interval). Observed ratios of 2.8 and 3.1, respectively, are obtained for the inner core and outer region at the impulsive phase peak[9]. These ratios are in disagreement with the purely chromospheric model at $T_c = 10^4$ K, which predicts a density insensitive ratio of ~ 8. The irradiation model, however, where only 50% of the 5000 Å continuum intensity arises in the chromosphere, predicts a ratio of 4, which might be acceptably similar to the observed values. Of course, the model ratios are sensitive to chromospheric temperature, so that at $T_c = 15{,}000$ K, and allowing for uncertainties in departures from LTE, the purely chromospheric model can produce ratios of 2.2 to 5.0, which bracket the observed values.

Turning next to the ratio of Balmer to Paschen continuum intensities measured with the MBP at 3610 and 4275 Å, the observed value of 8 (based on fluxes; see § 2.4) disagrees with the purely chromospheric model at 10^4 K, which predicts a ratio of 14, but is close to the irradiation model prediction of 7. Computations using $T_c = 15{,}000$ K in a purely chromospheric model leads to acceptable ratios of 7 to 9.

In summary, we are unable to choose between the purely chromospheric model and the irradiation model simply on the basis of the available spectral measurements, due to the uncertainties in the assumed values of chromospheric temperatures. Moreover, due to the relatively broad temperature maxima of the H_{fb} and H_{ff} continuum emissivity functions, the efficiency of the chromosphere in producing 5000 Å continuum is nearly identical at 10,000 and 15,000 K. Thus no argument based solely on emission measure requirements for producing 5000 Å continuum can be advanced for favoring any particular chromospheric temperature within this range. The available

[9] the Hα ± 3 Å intensity must be reduced by the continuum contribution at that wavelength. Because WLFs are generally observed to have a relatively flat spectrum at $\lambda > 4500$ Å (Neidig 1989), it can be reasonably assumed that the relative continuum enhancement in the vicinity of the Hα line will be the same as at 5000 Å.

optical measurements are, however, restrictive of the possible combinations of model type and chromospheric temperature: the choices are limited to a purely chromospheric model at ~15,000 K, at the one extreme, or an irradiation model with chromospheric temperature 10^4 K at the other. Because additional evidence discussed below seems to favor the irradiation model, we have therefore assumed 10^4 K as the appropriate chromospheric temperature in the calculations in the Appendix.

3.3. *Nonthermal Electron Power Sufficiency*

Using the purely chromospheric model the electron density n_e required to produce the observed 5000 Å peak intensity in the impulsive inner core is 6.9×10^{13} cm^{-3}. Under conditions of nearly full ionization, and assuming a static atmosphere, the latter electron density would be attained at atmospheric height $h \approx 890$ km above $\tau_{5000} = 1$ (see model C of Vernazza, Avrett, & Loeser 1981). However, because the H_{fb} and H_{ff} processes vary as n_e^2, the density derived from the optical continuum must correspond to the mean square density in the assumed 130 km thickness of the flare layer. Thus the top of the flare layer will actually be 75 km higher than the height where the mean square density is obtained, i.e., $h = 965$ km, corresponding to column density $N = 5.0 \times 10^{20}$ cm^{-2}. Nonthermal electrons penetrating to and below this atmospheric level require a minimum energy $E_e \approx (N/10^{17})^{1/2}$ keV (Bai 1982; Fisher, Canfield, & McClymont 1985a)—in this case ~70 keV. The power in nonthermal electrons above this cutoff energy is 8.5×10^{27} ergs s^{-1}, of which, if we assume the same fraction as applies to the optical outputs in Table 1, only 2.0×10^{27} ergs s^{-1} would enter the inner core. Thus the estimated available electron power is about a factor of 2 less than the inner core WLF output.

In the case of the irradiation model, where the chromospheric contribution is only half of the observed 5000 Å continuum intensity, the required electron density in the source is only 4.9×10^{13} cm^{-3} in the inner core and 3.2×10^{13} cm^{-3} in the outer region (see Appendix). (The former density is similar to the value 5.3×10^{13} cm^{-3} measured from spectral analysis of high Balmer lines in the 1981 April 24 WLF [Neidig 1983], which showed continuum intensity comparable to the March 7 event.) Using the same procedure as above, the resulting required electron cutoff energies are 60 and 48 keV, respectively, with corresponding electron powers as listed in Table 1. The WLF power requirements are now approximately satisfied in the inner core and amply satisfied in the outer region.

3.4. *Delays in the Optical Emissions*

The observed delay in the Hα wing emission relative to hard X-rays during the impulsive rise (Fig. 7) undoubtedly provides an important clue to the processes of energy transport and chromospheric heating. Because the Hα wing emission is assuredly dependent on electron density, its appearance must necessarily involve a chromospheric ionization work function and an associated time delay relative to the energy input. Lin & Hudson (1976) noted that for an initially cool chromosphere bombarded by high-energy electrons, nonthermal ionization dominates over thermal and radiative ionizations at column densities $N \geq 10^{20}$ cm^{-2} (as apply here) and temperatures $\leq 10^4$ K. Canfield & Gayley (1987) reached a similar conclusion and found, in their flare model, ionization time scales on the order of 1 s at densities several times 10^{13} cm^{-3} in the presence of nonthermal electron fluxes sufficient to produce bright Hα emission in flares. We calculate the nonthermal ionization time scale $t_i = 5.12 \times 10^{-11}\, n/Q$ (Lin & Hudson 1976) using a nonthermal electron energy deposition rate Q (ergs s^{-1} cm^{-3}) based on equation (9) of Fisher, Canfield, & McClymont (1985a) and assuming an electron beam cross section equal to the WLF area. For the purely chromospheric model, $t_i = 5$ s for the values of Q at the atmospheric heights corresponding to the optical source densities n required to produce the Hα emission, at all but the earliest moments during the impulsive rise in both the inner core and outer region. If we instead use the smaller density (and implied greater source height resulting from this smaller density) of the irradiation model, $t_i \approx 1$ s, which is quite close to the observed delay in the Hα wing emission. Also relevant to the delay in the Hα wing emission is the chromospheric condensation (if in fact the emission is so produced), whose formation time can be as short as 1 s for input electron fluxes $F_{20} = 10^{11}$ ergs s^{-1} cm^{-2} (Fisher et al. 1985a, b).

The delay in the 5000 Å continuum emission is harder to understand. The recombination time scale in Paschen continuum for a thermal distribution of electrons at 10^4 K is $t_r \approx 1.5 \times 10^{13}/n_e$ (e.g., Allen 1973), or only 0.3 and 0.5 s, respectively, for the electron densities estimated in the inner core and outer region. Of course these time scales would be longer under conditions of lower density, higher temperature, or non-Maxwellian electron velocity distribution resulting from nonthermal ionization. Appropriately long recombination time scales are obtained, for example, at $T > 50{,}000$ K or $n_e < 10^{13}$ cm^{-3}; however, the volumetric efficiency of the continuum processes is then greatly reduced, with the result that the line-of-sight thickness of the flare would exceed the observed lateral dimensions of the inner core. Even if chromospheric condensations (rather than nonthermal electrons, directly) are involved in producing the continuum, as suggested by Nagai (1980) and Livshits et al. (1981), there seems no explanation, apart from the recombination time scale, for the continuum delay relative to Hα wing (unless there exists a continuum-producing condensation too cold to produce Hα, and existing independently of the Hα-producing condensation).

Because the observed continuum delays are about an order of magnitude longer than predicted by recombination in a 10^4 K plasma, we are obliged to consider other processes, perhaps involving continuum sources outside the chromosphere. One possibility is the irradiated photosphere discussed above. The time scale for photospheric backwarming by absorption of chromospheric radiation is given by the ratio of the column work function in raising the photospheric temperature, to the input chromospheric flux. The latter quantity is derived in the Appendix. The work function is not known for the March 7 flare, although, as an approximation for this discussion, we rely on the atmospheric parameters in the irradiation model of Aboudarham & Henoux (1989). In their model the photospheric temperature is raised, via irradiation, between column depths 3×10^{23} and 3×10^{24} cm^{-2}. Assuming a thermal energy increment $(3/2)k\Delta T$ per hydrogen atom (with $\Delta T \approx 300$ K and 130 K, respectively, for the inner and outer regions; see Appendix), and neglecting ionization (which will remain small at these temperatures), we obtain a column work function 1.0×10^{11} ergs cm^{-2} and corresponding heating time scales of 7 and 16 s, respectively, for the inner core and outer region. These values, while perhaps not precisely applicable to the March 7 flare, nevertheless seem too long in comparison to the observed delays in the impulsive rise. In any case, because

the photospheric and chromospheric continua are estimated to be comparable in brightness, the delay of the two components combined—each with greatly different individual delays—could hardly be expected to closely reflect the chromospheric ionization profile. Yet this is precisely what is suggested by Figure 7.

4. DISCUSSION AND CONCLUSIONS

The observations presented here demonstrate several important refinements in flare observations. It is apparent that considerable advantage is gained in differentiating between the impulsive and gradual components by observing separately the kernel core and outer region. The differences in the time profiles and Hα red asymmetries in these two regions indicate that the classic signatures of explosive heating by nonthermal electrons, i.e., redshifted Hα line, broad line wings (evidenced here by exceptionally bright emission 3 Å from line center), and close temporal correlation with hard X-rays, are more evident in the inner core. Generally, the observations support the often assumed working hypothesis that the impulsive optical component is energized by nonthermal electrons. The strong similarity of the time variations in both hard X-rays and Hα wing to time variations in 5000 Å continuum further suggests that the association with nonthermal electrons might be extended to the WLF as well.

Central to the argument that nonthermal electrons are involved in producing the WLF is the question of power sufficiency. In the case of a purely chromospheric flare model, the power in the electron beam is estimated to be too small by a factor of 2 to balance the WLF radiative losses in the inner core impulsive phase. On the other hand, the assumption of an irradiation model, where the visible light flare continuum is approximately equally divided (at viewing angle 76°) between photospheric and chromospheric components, leads to probable power sufficiency. In view of various assumptions and uncertainties in the calculations, however, a more reliable conclusion is that power sufficiency *might* be achieved in either model, although more likely so in the case of the irradiation model. A major stumbling block encountered here is the method of determining the atmospheric height of the chromospheric flare source, which is derived from the density in a static atmosphere. The latter assumption may not be valid, considering the observed red asymmetry, which implies the existence of a chromospheric condensation which might modify the density in the region in question. In this case the estimated required densities might be obtained at higher altitudes.

The irradiation model may find support by virtue of its predicted 1 s chromospheric ionization time scale, which is in better agreement with the observed Hα wing delay than the longer ionization time scale expected from the higher densities and greater depths of the purely chromospheric WLF source. The observed lag is in good agreement with earlier predictions by Canfield & Gayley (1987) and bolsters their claim that observations at several points in the Hα line wings can provide valuable diagnostics for discriminating between chromospheric flare heating mechanisms. We point out, however, that the relatively good agreement between the predicted and observed lag may be somewhat fortuitous in this case because the chromospheric ionization time scale is much shorter than the time scale (≈ 10 s) for the rise in electron flux, i.e., the rise is not truly impulsive; thus the calculation of the expected Hα wing lag might require time-dependent modeling of the electron density, taking into account both the thermal and nonthermal ionization and recombination rates. Also, the role of chromospheric condensations in contributing to the lag remains unknown in the presence of electron fluxes much larger than have been assumed in hydrodynamic models available thus far.

The lag in the 5000 Å continuum emission is a new phenomenon and will doubtless place further constraints on flare impulsive phase models. The formation of chromospheric continua via recombination will inevitably result from the increased ionization responsible for the emission in the Hα line wings. However, the observed lag of the continuum relative to the Hα wing may be longer than the expected chromospheric recombination time scale and possibly shorter than the photospheric heating time scale according to the irradiation model. Thus a satisfactory explanation for the continuum lag has not been obtained here. If the photospheric heating time scale is on the order of 10 s, as estimated here, then the photospheric response to the impulsive chromospheric component might be confused with the flare gradual emission which peaks 15 s after the impulsive phase. In fact, it is interesting to consider to what extent the gradual emission itself might represent the photospheric irradiation component we discuss. The fact that the gradual emission dominates the continuum in the outer region of the flare kernel might support this conjecture, as the effect of irradiation is expected to be spread out somewhat, relative to its overlying chromospheric source. Arguing against this possibility is the existence of a gradual chromospheric component as well (the Hα emission), beginning well before the impulsive phase, as does the WLF continuum. Finally, we note that if long delays in the irradiated continuum component do occur, then serious error may be encountered in assigning to the photosphere 50% of the observed continuum at the impulsive peak.

We are unable to provide unequivocal evidence for heating of the WLF source by nonthermal electrons; obviously, several important questions arising here will have to be explored by means of detailed modeling and more comprehensive data before any such definitive conclusion can be reached. On the other hand, the observations presented here are in large measure consistent with nonthermal electron heating of the chromosphere, as seems especially evident in the impulsive phase. A remaining question is why only this one hard X-ray peak was associated with white-light emission, while other, more energetic peaks with harder electron spectra (occurring earlier) were not. The answer may be that the electron beam cross sections in the kernels associated with these other hard X-ray peaks were larger, leading to reduced electron fluxes at these locations. As for the gradual emission, the presence of an associated hard X-ray component is difficult to confirm; and the possible absence of redshift in the gradual peak lends no support for nonthermal electron heating in the gradual phase. The absence of a gradual phase redshift would be expected if the electron flux were less than the critical value required for explosive heating and condensation formation ($F_{20} \approx 3 \times 10^{10}$ ergs s^{-1} cm^{-2}, according to Fisher et al. 1985a); however, we estimate F_{20} to exceed this value by more than an order of magnitude in the outer region of the flare kernel.

The authors express their appreciation to E. Avrett, R. Canfield, and G. Fisher for useful discussions related to this work. We thank J. Harvey for providing magnetograms of the active region.

APPENDIX

CALCULATION OF THE TOTAL WHITE-LIGHT POWER AND THE VARIATION OF FLARE INTENSITY WITH VIEWING ANGLE

In this Appendix we derive relationships for estimating the wavelength-integrated WLF power in an irradiation model, as well as the variation with viewing angle of the intensity contributions of the flare chromospheric and photospheric components.

We consider an optically thin chromospheric flare slab irradiating an underlying photospheric slab. In the case where the lateral dimensions of these slabs are large in comparison to their height separation, the wavelength-integrated flux $F_{c,f}$ emerging from the chromospheric flare slab in the downward hemisphere will be approximately equal to the irradiating flux incident on the photospheric slab. This energy input will increase the photospheric temperature by some amount, thereby increasing the photospheric flux from its quiet sun value $F_{p,q}$ to a flare value $F_{p,f}$. Energy balance requires

$$F_{c,f} = F_{p,f} - F_{p,q} . \tag{A1}$$

In the optically thin case the specific intensity emergent from the flare chromosphere at angle θ from the normal is related to the intensity in the normal direction by

$$I_{c,f,\lambda}(\theta) = I_{c,f,\lambda}(0°)/\cos\theta . \tag{A2}$$

Integrating this intensity over wavelength and one hemisphere of solid angle yields the chromospheric flare flux

$$F_{c,f} = 2\pi \int I_{c,f,\lambda}(0°)d\lambda . \tag{A3}$$

Multiplying and dividing by the chromospheric intensity at 5000 Å (subscript 5 will be used to denote 5000 Å) in the normal direction, $I_{c,f,5}(0°)$, we obtain

$$F_{c,f} = 2\pi I_{c,f,5}(0°)\Delta\lambda , \tag{A4}$$

where $\Delta\lambda \equiv \int [I_{c,f,\lambda}(0°)/I_{c,f,5}(0°)]d\lambda \approx 2 \times 10^{-4}$ cm is the effective spectral width of the flare chromospheric emission, calculated for the conditions assumed for the chromospheric flare (§ 3.2). The spectral width $\Delta\lambda$ is virtually independent of the density in the flare chromosphere as long as the source is optically thin (as in the cases considered here). The numerical value of $I_{c,f,5}(0°)$ is unknown, and its solution is the key element of the present exercise. The computed chromospheric flare spectrum, using the solution value $I_{c,f,5}(0)$ derived below, is shown in Figure 8; the contribution from the Lyman continuum has not been included in this calculation.

The right side of equation (A1) can be expressed in terms of the effective temperatures of the flare and quiet photospheres:

$$\begin{aligned} F_{p,f} - F_{p,q} &= \sigma(T_{\mathrm{eff},f}^4 - T_{\mathrm{eff},q}^4) \\ &= \sigma(r_f T_f^4 - r_q 6050^4) , \end{aligned} \tag{A5}$$

where on the second line the effective temperatures have been converted to radiation temperatures (T_f, and $T_q = 6050$ K) using the ratios (r_f and r_q) of mean to normal intensity in the flare and quiet photospheres. Equations (A4) and (A5) yield:

$$T_f = r_f^{-1/4}[2\pi\sigma^{-1} I_{c,f,5}(0°)\Delta\lambda + r_q 6050^4]^{1/4} . \tag{A6}$$

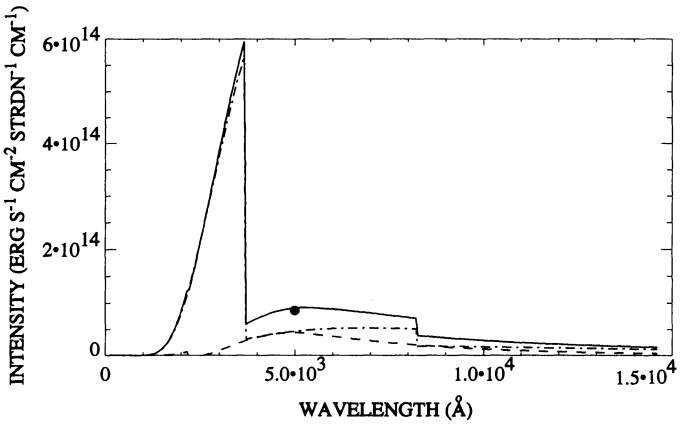

FIG. 8.—Model spectrum $[I_f(\lambda) - I_0(\lambda)]$ of the kernel inner core, computed from the irradiation model at a viewing angle of 76°. *Dashed curve:* the photospheric component, given by the difference between eq. (A7) as evaluated at $T_f = 6363$ K and at 6050 K; a wavelength-dependent quiet Sun limb-darkening function has been applied in each case. *Dash-dotted curve:* the chromospheric component, computed according to the model of § 3.2, in this case with $n_e = 4.9 \times 10^{13}$ cm^{-3} cm^{-3}, $T_e = 10^4$ K, departure coefficients for second- and third-level hydrogen atoms are 1.74 and 1.24, respectively (all higher levels are assumed to be in LTE), and vertical thickness of chromospheric flare layer 130 km. *Solid curve:* the sum of the photospheric and chromospheric components. The dot shows the observed WLF intensity at 5000 Å.

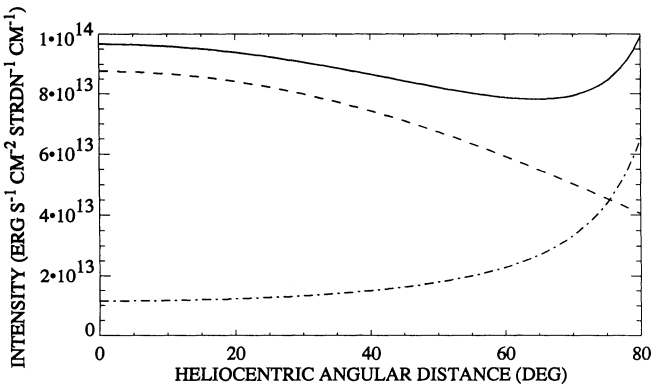

FIG. 9.—The 5000 Å continuum intensity $[I_f - I_o]$ in the inner core as a function of viewing angle, computed from the irradiation model and assuming the same physical conditions as in Fig. 8. Shown are the photospheric component (*dashed curve*), the chromospheric component (*dash-dotted*), and the emergent flare intensity enhancement (*solid curve*) given by the difference between eq. (A8) and the quiet Sun background intensity. The curves have been terminated at $\theta = 80°$ due to the breakdown of plane-parallel geometry near the limb.

The photospheric flare intensity can be approximated in terms of T_f by

$$I_{p,f,\lambda}(\theta) = B_\lambda(T_f) l_f(\lambda,\theta) \tag{A7}$$

where B_λ is the Planck function and $l_f(\lambda, \theta) \equiv I_{p,f,\lambda}(\theta)/I_{p,f,\lambda}(0°)$, analogous to the definition for photospheric limb darkening. Neither $l_f(\lambda, \theta)$ in equation (A7) nor r_f in equation (A6) is known, although the respective quiet Sun values are given by (Allen 1973): $l_q(\lambda, \theta) = 1 - u_1(\lambda) + u_1(\lambda) \cos\theta$, with $u_1 = 0.65$ at 5000 Å, and $r_q = 0.83$. In the flare these quantities might be different, depending on the temperature gradient in the flare photosphere. However, in numerous trial solutions for the θ-dependent flare intensity derived below, it was found that small changes from the quiet Sun values of r and $l(\lambda, \theta)$ resulted in a θ-dependency of total flare intensity (for $\theta > 50°$) which is in disagreement with observed statistics on WLF center-to-limb intensity distributions (Neidig, Wiborg, & Gilliam 1993). Therefore we assume quiet Sun values for r_f and $I_f(\lambda, \theta)$.

The emergent intensity from the flare can be expressed in terms of the radiative transfer equation for a homogeneous chromospheric source:

$$I_{f,\lambda}(\theta) = I_{p,f,\lambda}(\theta) e^{-\Delta\tau_\lambda(\theta)} + S_\lambda(1 - e^{-\Delta\tau_\lambda(\theta)}) , \tag{A8}$$

where $\Delta\tau_\lambda(\theta)$ and S_λ are the optical thickness and radiative source function of the chromospheric flare layer. The latter quantities are computed from the chromospheric model (§ 3.2) after the electron density n_e has been specified. The objective is to select a density n_e leading to $I_{c,f,5}(0°)$ (and hence to T_f and $I_{p,f,\lambda}$) that will result in an emergent flare intensity $I_{f,5}(76°)$ (from eq. [A8]) identical with observation. For the kernel core the result is a chromospheric electron density $n_e = 4.9 \times 10^{13}$ cm^{-3} and intensity $I_{c,f,5}(0°) = 1.14 \times 10^{13}$ ergs s^{-1} cm^{-2} sr^{-1} cm^{-1}, with corresponding $T_f = 6363$ K. Figure 9 plots $I_{p,f,5}(\theta) - I_{p,q,5}(\theta)$ and $I_{c,f,5}(\theta)$ along with the emergent flare intensity $I_{f,5}(\theta)$. In the case where the chromospheric emission is optically thin and $S_5 \gg I_{p,f,5}(\theta)$ the emergent flare intensity will be nearly identical to the sum of $[I_{p,f,5}(\theta) - I_{p,q,5}(\theta)]$ and $I_{c,f,5}(\theta)$, which then represent the individual contributions from the flare photosphere and chromosphere.

In the irradiation model all of the WLF power originally derives from the chromosphere. Thus the total radiative output in the near-ultraviolet, visible, and near-infrared continua is simply the θ-dependent chromospheric intensity integrated over 4π sr and multiplied by the flare area a; this is equivalent to multiplying equation (A4) by a quantity $2a$:

$$P_{\rm WLF} = 4\pi a I_{c,f,5}(0°)\Delta\lambda . \tag{A9}$$

For the core region we obtain $P_{\rm WLF} \approx 3.7 \times 10^{27}$ ergs s^{-1}. The same exercise is repeated for the outer region of the flare, resulting in $n_e = 3.2 \times 10^{13}$ cm^{-3}, $I_{c,f,5}(0°) = 4.9 \times 10^{12}$ ergs^{-1} s^{-1} cm^{-2} sr^{-1} cm^{-1}, $T_f = 6178$ K, and $P_{\rm WLF} \approx 7.5 \times 10^{27}$ ergs s^{-1} at the time of the impulsive peak.

REFERENCES

Aboudarham, J., & Henoux, J. C. 1989, Sol. Phys, 121, 19
Allen, C. W. 1973, Astrophysical Quantities (London: Athlone)
Bai, T. 1982, ApJ, 259, 341
Beckers, J. M., Bridges, C. A., & Gilliam, L. B. 1976, A High Resolution Spectral Atlas of Solar Irradiance from 380 to 700 Nanometers, AFGL-TR-76-0126(II) (Hanscom AFB, MA)
Boyer, R., Machado, M. E., Rust, D. M. & Sotirovski, P. 1985, Sol. Phys, 98, 255
Brown, J. C. 1971, Sol. Phys, 18, 489
Canfield, R. C., & Gayley, K. G. 1987, ApJ, 322, 999
Canfield, R. C., & Gunkler, T. A. 1985, ApJ, 288, 353
Canfield, R. C., Gunkler, T. A., & Ricchiazzi, P. J. 1984, ApJ, 282, 296
Canfield, R. C., et al. 1986, Energetic Phenomena on the Sun, ed. M. R. Kundu & B. Woodgate, NASA CP 2439
De Feiter, L. 1966, Analysis of the Balmer Spectrum of Solar Flares, Recherches Astron. L'Observ. D'Utrecht, 18(2) (Dordrecht: Reidel)
Fisher, G. H., Canfield, R. C., & McClymont, A. N. 1985a, ApJ, 289, 414
———. 1985b, ApJ, 289, 434
Gan, W. Q., Rieger, E., Zhang, H. Q., & Fang, C. 1991, ApJ, 397, 694
Gayley, K. G., & Canfield, R. C. 1991, ApJ, 380, 660
Hawley, S. L., & Fisher, G. H. 1992, ApJS, 78, 565
Henoux, J. C. 1991, in Conf. Proc. Solar Polarimetry, ed. L. J. November (Sunspot: National Solar Obs.), 285
Kämpfer, N., & Magun, A. 1983, ApJ, 274, 910

Kurokawa, H., Takakura, T., & Ohki, K. 1988, PASJ, 40, 357
Lin, R. P., & Hudson, H. S. 1976, Sol. Phys., 50, 153
Lin, R. P., & Schwartz, R. A. 1987, ApJ, 312, 462
Livshits, M. A., Badalyan, O. G., Kosovichev, A. G., & Katsova, M. M. 1981, Sol. Phys., 73, 268
Machado, M. E., et al. 1986, in Conf. Proc. The Lower Atmosphere of Solar Flares, ed. D. F. Neidig (Sunspot, NM: National Solar Obs.), 483
Machado, M. E., Emslie, A. G., & Avrett, E. H. 1989, Sol. Phys., 124, 303
Mauas, P. J. 1990, ApJS, 74, 609
Nagai, F. 1980, Sol. Phys., 68, 351
Neidig, D. F. 1981, Sol. Phys., 70, 129
———. 1983, Sol. Phys., 85, 285
———. 1989, Sol. Phys, 121, 261
Neidig, D. F., & Beckers, J. M. 1983, S&T, 65(3), 226
Neidig, D. F., & Kane, S. R. 1993, Sol. Phys., in press
Neidig, D. F., Kane, S. R., Hrovat, M., & Grosser, H. 1989, BAAS, 21, 846
Neidig, D. F., Wiborg, P. H., & Gilliam, L. B. 1993, Sol. Phys., in press
Niblack, W. 1986, An Introduction to Digital Image Processing (London: Prentice Hall Internat.)
Nitta, N., Kiplinger, A. L., & Kai, K. 1989, ApJ, 337, 1003
Orwig, L. E., Frost, K. J., & Dennis, B. R. 1980, Sol. Phys., 65, 25
Schwartz, R. A., Orwig, L. E., Dennis, B. R., Ling, J. C., & Wheaton, W. A. 1991, ApJ, 376, 312
Svestka, Z. 1965, Adv. Astron. Astrophys., 3, 119
Vernazza, J. E., Avrett, E. H., & Loeser, R. 1981, ApJS, 45, 635
Wülser, J. P., & Marti, H. 1989, ApJ, 341, 1088
Zarro, D. M., & Canfield, R. C. 1989, ApJ, 338, L33